



Kent Academic Repository

Chauhan, Manish, Samal, Manash, Tej, Anandmayee and Froebrich, Dirk (2024)
Search for protostellar jets with UWISH2 in the molecular cloud complexes Vulpecula and IRDC G53.2. Monthly Notices of the Royal Astronomical Society, 530 (1).
pp. 515-529. ISSN 0035-8711.

Downloaded from

<https://kar.kent.ac.uk/105505/> The University of Kent's Academic Repository KAR

The version of record is available from

<https://doi.org/10.1093/mnras/stae846>

This document version

Author's Accepted Manuscript

DOI for this version

Licence for this version

CC BY (Attribution)

Additional information

Versions of research works

Versions of Record

If this version is the version of record, it is the same as the published version available on the publisher's web site. Cite as the published version.

Author Accepted Manuscripts

If this document is identified as the Author Accepted Manuscript it is the version after peer review but before type setting, copy editing or publisher branding. Cite as Surname, Initial. (Year) 'Title of article'. To be published in **Title of Journal**, Volume and issue numbers [peer-reviewed accepted version]. Available at: DOI or URL (Accessed: date).

Enquiries

If you have questions about this document contact ResearchSupport@kent.ac.uk. Please include the URL of the record in KAR. If you believe that your, or a third party's rights have been compromised through this document please see our [Take Down policy](https://www.kent.ac.uk/guides/kar-the-kent-academic-repository#policies) (available from <https://www.kent.ac.uk/guides/kar-the-kent-academic-repository#policies>).

Search for protostellar jets with UWISH2 in the molecular cloud complexes Vulpecula and IRDC G53.2

Manish Chauhan,^{1*} Manash Samal,^{2†} Anandmayee Tej,^{1‡} Dirk Froebrich³

¹Indian Institute of Space Science and Technology, Thiruvananthapuram, India

²Physical Research Laboratory, Ahmedabad, India

³University of Kent, Canterbury, UK

*currently working at Space Applications Centre, ISRO, Ahmedabad, India

Accepted XXX. Received YYY; in original form ZZZ

ABSTRACT

Jets and outflows are the early signposts of stellar birth. Using the UKIRT Wide Field Infrared Survey for H₂ (UWISH2) at 2.12 μm , 127 outflows are identified in molecular cloud complexes Vulpecula OB1 and IRDC G53.2 covering 12 square degrees of the Galactic plane. Using multi-wavelength datasets, from 1.2 to 70 μm , 79 young stellar objects (YSOs) are proposed as potential driving sources, where, $\sim 79\%$ are likely Class 0/I protostars, 17% are Class II YSOs and the remaining 4% are Class III YSOs. The outflows are characterized in terms of their length, flux, luminosity and knot-spacing. The identified outflows have a median lobe length of 0.22 pc and 0.17 pc for outflows in Vulpecula OB1 and IRDC G53.2, respectively. Our analysis, from the knot spacing, reveals a typical ejection frequency of ~ 1.2 kyr suggesting an intermediate type between the FU-Ori and EX-Ori type of eruptions in both cloud complexes. Furthermore, the physical parameters of the driving sources are obtained by performing radiative transfer modelling to the observed spectral energy distributions (SEDs), which suggest that the outflows are driven by intermediate mass stars. Various observed trends between the outflow properties and the corresponding driving sources, and various interesting outflows and star forming sites, including sites of triggered star formation and protocluster forming clump with clusters of jets, are discussed. The obtained results and the identified jet-bearing protostellar sample will pave the way to understand many aspects of outflows with future high-resolution observations.

Key words: stars: formation – stars: jets – ISM: jets and outflows – infrared: stars

1 INTRODUCTION

Jets and outflows are ubiquitous in star forming regions and are important signposts of stellar birth. Outflows represent entrained ambient interstellar medium (ISM) surrounding high velocity ejections from YSOs, and thus, provide fossil record of the associated mass accretion process (Hartmann et al. 1998). This picture is supported by numerous theoretical and observational studies spanning more than a century (e.g. Burnham 1890; Herbig 1950; Haro 1952; Snell et al. 1980).

The protostellar jets can have velocities of a few tens to a hundred kms^{-1} (Reipurth & Bally 2001; Lee 2020) which allow them to carve out parsec-scale cavities in protostellar envelopes. Thus, they broadly influence the star formation process and growth of protostars or protoclusters in a variety of ways (see reviews by Bally 2016; Anglada et al. 2018; Ray & Ferreira 2021). For example, observations and numerical simulations suggest that protostellar jets/outflows inject a significant amount of energy and momentum into their surroundings and have a profound impact on their host cores/clumps (e.g. Arce et al. 2010; Plunkett et al. 2013), thus, influencing the star-formation efficiency therein (e.g. Nakamura & Li 2007; Machida &

Hosokawa 2013; Wang et al. 2010; Federrath et al. 2014; Offner & Arce 2014; Krumholz & Federrath 2019). Similarly, theoretical as well as simulation works suggest that short outbursts with high accretion rate can mitigate the long-standing "luminosity problem" (Kenyon et al. 1990; Offner & McKee 2011). Since, accretion and ejection are strongly coupled, episodic accretion events can be indirectly detected by the episodic outflows they trigger (Arce et al. 2007; Vorobyov et al. 2018; Rohde et al. 2019). Thus, the spacing and kinematics of outflow bullets (or knots) and their properties can provide insights into the underlying episodic protostellar accretion. Numerical simulations also suggest that presence of a companion and interaction with sibling stars can strongly impact the outflow axis and shapes (e.g. Falle & Raga 1993; Terquem et al. 1999; Bate et al. 2000). Testing and/or confirming these predictions lies critically in finding and characterizing a statistically robust sample of jets/outflows of different structures, morphologies, and evolutionary status, and linking them to the properties, characteristics, and motions of their driving sources or cores.

Emission from jets/outflows can be probed over a wide range of wavelengths. Different frequencies trace the emission from different regions of the shock-excited ISM resulting from collision with jets (Bally 2016). Observation of optical emission associated with these jets/outflows, dubbed as Herbig-Haro objects, is limited mostly to nearby star forming regions or massive outflows owing to large ex-

* E-mail: manish.chauhan@outlook.in

† E-mail: manash@prl.res.in

‡ E-mail: tej@iist.ac.in

tion towards Galactic star-forming clouds. Thus, jets/outflows in the Galactic plane are best traced at longer wavelengths as the effects of extinction is significantly reduced compared to the optical domain (e.g. Stanke et al. 2002; Davis et al. 2010; Hartigan et al. 2015; Reiter et al. 2017, 2022).

Large sample of jet-bearing YSOs, similar to Makin & Froebrich (2018), are necessary to obtain an in-depth knowledge of jets/outflows and their role in star formation. The UWISH2 survey (Froebrich et al. 2011) is an excellent database to directly probe jets/outflows in the Galactic plane. This is an unbiased narrow-band survey of the first Galactic quadrant ($10^\circ < l < 65^\circ$, $|b| < +1.3^\circ$) centered on the H_2 ro-vibrational 1-0S(1) transition at $2.12 \mu\text{m}$ which is an excellent tracer of shock-excited, hot ($\sim 2000 \text{ K}$), and dense ($n \geq 10^3 \text{ cm}^{-3}$) molecular gas. The survey was further extended to cover the Auriga and Cygnus region (see Froebrich et al. 2015, F15 hereafter). A number of surveys in the H_2 1-0S(1) line transition at $2.12 \mu\text{m}$, using data from UWISH2, reveal a large population of molecular hydrogen emission-line objects (MHOs) or outflows associated with YSOs in Galactic star-forming regions (Ioannidis & Froebrich 2012a; Makin & Froebrich 2018; Makin 2019).

In this paper, we conduct an extensive study of jets/outflows in two star-forming complexes, namely the Vulpecula OB association (hereafter Vul OB1) and the InfraRed Dark Cloud located at Galactic coordinates ($l \sim 53.2^\circ$, $b \sim 0.0^\circ$) (hereafter IRDC G53.2). The analysis is carried out using UWISH2 data in combination with multi-wavelength data retrieved from various archives (discussed in Section 2). The two target regions provide excellent opportunity to study star formation in massive ($\sim 10^5 M_\odot$) molecular clouds in the Galactic plane (see Wang et al. 2020; Kohno et al. 2022). A large number of H_2 emission features are identified in these regions (refer to Section 3 for more details). IRDC G53.2 is a 45 pc long filamentary cloud located at a distance of 1.7 kpc with a rich YSO population of 373 candidate YSOs (Kim et al. 2015). Vul OB1 ($l \sim 60.2^\circ$, $b \sim -0.2^\circ$) is an active star-forming site located at a distance of 2.3 kpc with around 856 YSO candidates identified by Billot et al. (2010). Vul OB1 also hosts the young open cluster NGC 6823 with an estimated age of $4 \pm 2 \text{ Myr}$ (Bica et al. 2008). Furthermore, three young HII regions are also seen to be associated with this region (Sh2-86, Sh2-87 and Sh2-88; Sharpless 1959). Vul OB1 is affected by strong feedback from nearly 100 massive OB stars found in the region (Reed 2003). As a result, several feedback sculpted structures such as pillars or elephant-trunk like features have been identified in the complex (e.g. Billot et al. 2010). These pillars are important sites for studying triggered star formation (e.g. Billot et al. 2010; Panwar et al. 2019), and detection of young outflows can possibly unravel induced star formation in such regions.

In presenting the study, we structure the paper as follows. The data sets used in the analysis are discussed in Section 2. The identification of MHOs, the likely driving source candidates and the distribution of various physical parameters of the MHOs and their driving sources are detailed in Section 3. Discussion on the correlations between the properties of the MHOs with the corresponding physical properties of the driving source candidates is given in Section 4. In Section 5, we discuss a few interesting star-forming sites identified in this study. The results of the study are summarized in Section 6.

2 DATA SETS

2.1 NIR data from UWISH2 and UKIDSS

The UWISH2 survey mapped the First Galactic Quadrant of the Galactic plane using the Wide-Field Camera (WFCAM) at the United

Kingdom Infrared Telescope (UKIRT) providing narrow band images centered on the H_2 1-0S(1) transition. The survey has a 5σ detection limit of 18 magnitudes in K-band and surface brightness limit of $10^{-19} \text{ Wm}^{-2} \text{ arcsec}^{-2}$ (Froebrich et al. 2011). Continuum-subtracted H_2 line images retrieved from the UWISH2 archive¹ are used for the identification of jets/outflows. These images are obtained by subtracting the scaled K-band continuum images from the H_2 narrow-band images.

H_2 line emission from jets/knots appear as positive features in the continuum-subtracted images. Several discrete jets/knots in a region can be associated to a coherent outflow. In this work, we use the discrete H_2 line-emission source catalogue for shock-excited jets by Froebrich et al. (2015) to identify outflows of the studied complexes. We also utilize near-infrared (J, H and K band) photometric data and images taken as part of the UKIRT Infrared Deep Sky Survey's Galactic Plane Survey (UKIDSS-GPS, Lucas et al. 2008) retrieved from the WFCAM Science Archive². J, H, and K-band photometric data are used for construction of extinction maps with the PNICER algorithm (refer Section 3.2).

2.2 CO data

CO position-velocity data cubes from Dame et al. (2001)³ and Jackson et al. (2006)⁴ have been used to study the structure and extent of the Vul OB1 and IRDC G53.2 complexes, respectively. For IRDC G53.2, we use the ^{13}CO ($J=1 \rightarrow 0$) transition data from the Galactic Ring Survey (GRS, Jackson et al. 2006) with a spatial resolution of $46''$ and velocity resolution of 0.21 km s^{-1} . In case of Vul OB1 complex, lower resolution (angular resolution of $\sim 7.5'$ and velocity resolution of 0.65 km s^{-1}) CO data cubes from Dame et al. (2001)⁵ have been used as the cloud falls outside the coverage of GRS ($18^\circ < l < 55.7^\circ$ and $|b| < 1^\circ$). The CO data is primarily used to define the outer extent of these clouds based on the integrated CO-emissions.

2.3 Mid-Infrared data from *Spitzer* Space Telescope

Mid-Infrared (MIR) data from the Galactic Legacy Infrared Mid-plane Survey Extraordinaire (GLIMPSE, Benjamin et al. 2003; Churchwell et al. 2009) in four IRAC bands between 3.6 and $8.0 \mu\text{m}$ and the MIPS GALactic plane survey at $24 \mu\text{m}$ (MIPSGAL, Carey et al. 2009) of the *Spitzer* Space Telescope have been used for identification of driving source candidates for the identified jets/outflows. We used the Infrared Science Archive's (IRSA) cutout service to obtain archival data for GLIMPSE and MIPSGAL surveys⁶. The data products offer a spatial resolution of $2''$ and $6''$ for the *Spitzer* IRAC and MIPS band, respectively.

2.4 Far-Infrared data from Hi-GAL survey

Far-Infrared (FIR) data from the *Herschel* Infrared Galactic Plane Survey (Hi-GAL, Molinari et al. 2010) are used in this study. The datasets retrieved from the science archives of the *Herschel* Space Observatory⁷ include the Highly Processed Data Product (HPDP)

¹ <http://astro.kent.ac.uk/uwish2/>

² <https://wsa.roe.ac.uk/>

³ <https://www.cfa.harvard.edu/rtcd/CO/CompositeSurveys/>

⁴ https://www.bu.edu/galacticring/new_data.html

⁵ <https://www.cfa.harvard.edu/rtcd/CO/>

⁶ <https://irsa.ipac.caltech.edu/applications/Cutouts/>

⁷ <http://archives.esac.esa.int/hsa/wsa/>

images from the Photodetector Array Camera and Spectrometer (PACS; 70 μm and 160 μm) and the Spectral and Photometric Imaging Receiver (SPIRE; 250 μm , 350 μm , and 500 μm). The images have spatial resolutions of 6'', 12'', 17'', 24'', and 35'' at 70, 160, 250, 350, and 500 μm , respectively. FIR data are used to identify deeply embedded YSO candidates and to investigate the nature of the driving sources.

2.5 Additional Data

We also use images from the APEX Telescope Large Area Survey of the Galaxy (ATLASGAL, Schuller et al. 2009) and the compact source catalogue of Csengeri et al. (2014) at 870 μm , to examine the cold dust emission and identify clumps/cores in the vicinity of jets/knots. The 870 μm images, with a spatial resolution of 19.2'', are downloaded for the two complexes under study from the ATLASGAL Database Server⁸. It should be noted that this catalogue, however, is limited to clumps with masses greater than 650 M_{\odot} . In addition, we have also examined the SiO emission catalogue of Csengeri et al. (2016) around clumps. SiO emission is believed to originate from shock-excitation and can trace outflows from the youngest Class 0/I sources (see Samal et al. 2018, and references therein).

3 ANALYSIS AND RESULTS

3.1 Identification of jets/outflows and driving source candidates

Studies of MHOs using UWISH2 data have revealed that majority of the regions observed by UWISH2 are devoid of outflows, $\sim 2/3$ rd of the survey field in some cases (e.g. Ioannidis & Froebrich 2012a). Keeping this in mind, we retrieve only the continuum-subtracted image tiles from the UWISH2 website with identified discrete H_2 line-emission sources from the F15 catalogue. In order to avoid any contamination or artefacts from bright stars, fluorescent emission, and other shock-excited features, we use only the features labelled as 'jets' in the F15 catalogue. Jets/outflows from YSOs appear as chains of H_2 emission knots. The nature of these knots will be discussed in a later section (Section 4.2). Figure 1 is an exemplar of aligned discrete H_2 knots in a star-forming site in Vul OB1, seen in the H_2 -K image. The H_2 1-0S(1) line-emission also manifests as red features in the JHH₂ colour-composite images, as seen in the lower panel of Figure 1. The JHH₂ colour-composite images are used to confirm the classification of the H_2 features as jets and any possible contamination is removed.

Chains of H_2 features are linked to a single outflow based on the proximity and alignment of these knots. Following the scheme proposed by Davis et al. (2010), all morphologically well-connected H_2 emission objects are considered as a single MHO or outflow. The remaining discrete and isolated H_2 features are also considered as unique MHOs. As an example, in Figure 1, all the six discrete emission features are considered to be part of a single MHO in our study. Using this approach, we identified a total of 127 MHOs in our study region, with Vul OB1 hosting 39% of the identified outflows and IRDC G53.2 having 61% of the outflows. Detailed discussion on individual MHOs is given in the online material. While velocity information of individual knots are required to confirm their association, the morphology seen gives a strong indication that in all likelihood the proposed association would be correct.

⁸ http://atlasgal.mpifr-bonn.mpg.de/cgi-bin/ATLASGAL_DATABASE.cgi

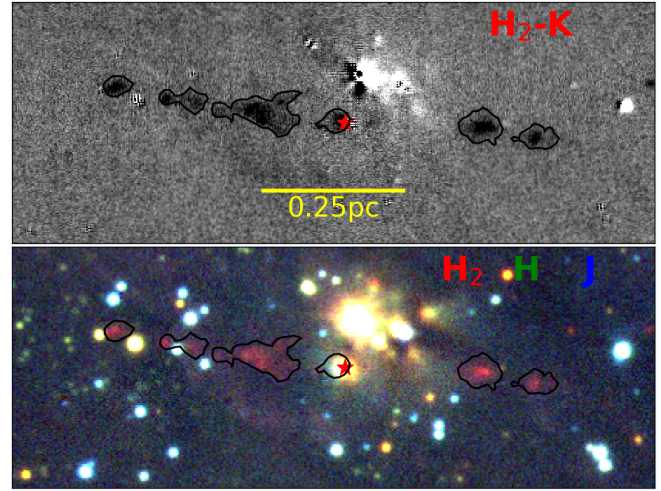


Figure 1. Example of a jet identified in Vul OB1. The top image is the continuum-subtracted (H_2 -K) image from UWISH2 data and bottom panel shows the JHH₂ colour-composite image. The black contours shown are the extended H_2 line-emission sources from F15 catalogue. The location of the driving source is marked by a red star.

Accurate identification and classification of the driving source candidates becomes crucial while estimating the physical properties such as length, luminosity, morphology and dynamical time of identified MHOs. As is well established, MHOs are driven by actively accreting YSOs that are distinguishable by their IR colours (see Varicatt et al. 2010, 2013; Froebrich & Makin 2016; Samal et al. 2018). Using *Spitzer* IRAC and MIPS band photometry and following the spectral index based classification criteria from Greene et al. (1994), the young stellar population in Vul OB1 and IRDC G53.2 have been classified by Billot et al. (2010) and Kim et al. (2015), respectively. Along with these YSO catalogs, we create multiple colour-composite images, similar to those displayed in Figure 2, for the identification of the driving source candidates for the identified MHOs. These include, (1) JHH₂, (2) IRAC 3.6 μm , 4.5 μm and 8.0 μm , (3) IRAC 4.5 μm , 8.0 μm and MIPS 24 μm , and (4) SPIRE 250 μm , 350 μm , 500 μm , colour-composite images. In addition, PACS 70 μm images overlaid with contours of ATLASGAL 870 μm emission are also utilized. Presence of cold dust emission traced at 870 μm near the jets/knots suggest that the driving sources are very likely embedded in dusty clumps or cores. YSOs identified from Billot et al. (2010); Kim et al. (2015) have been depicted by circles with Class 0/I YSOs in red, Class II YSOs in magenta, and Class III YSOs in orange.

It should be noted that the deeply embedded protostars (e.g. Class 0 YSOs) are often faint or lack detection in the IRAC bands and hence may have been excluded from the YSO catalogues of Billot et al. (2010); Kim et al. (2015). These sources, however, are bright at longer wavelengths and appear as bright sources in the MIPS 24 μm and PACS 70 μm bands (see Figure 2). In order to identify these deeply embedded sources, we formulate a classification scheme based on their [24]-[70] colour. In Figure 3, we plot the protostars identified as part of the Herschel Orion Protostars Survey (Stutz et al. 2013; Manoj et al. 2013, HOPS). As seen in the figure, majority of the HOPS protostars (98%) are found to have colours, $\log\left(\frac{\lambda F_{\lambda 70}}{\lambda F_{\lambda 24}}\right) > -0.5$. Using this colour cut, we identify 9 deeply embedded YSOs lacking detection in the *Spitzer* IRAC bands in Vul OB1 and IRDC G53.2. These are highlighted as red stars in the figure. YSOs with IRAC detection are also shown in the plot as blue stars. All the driving

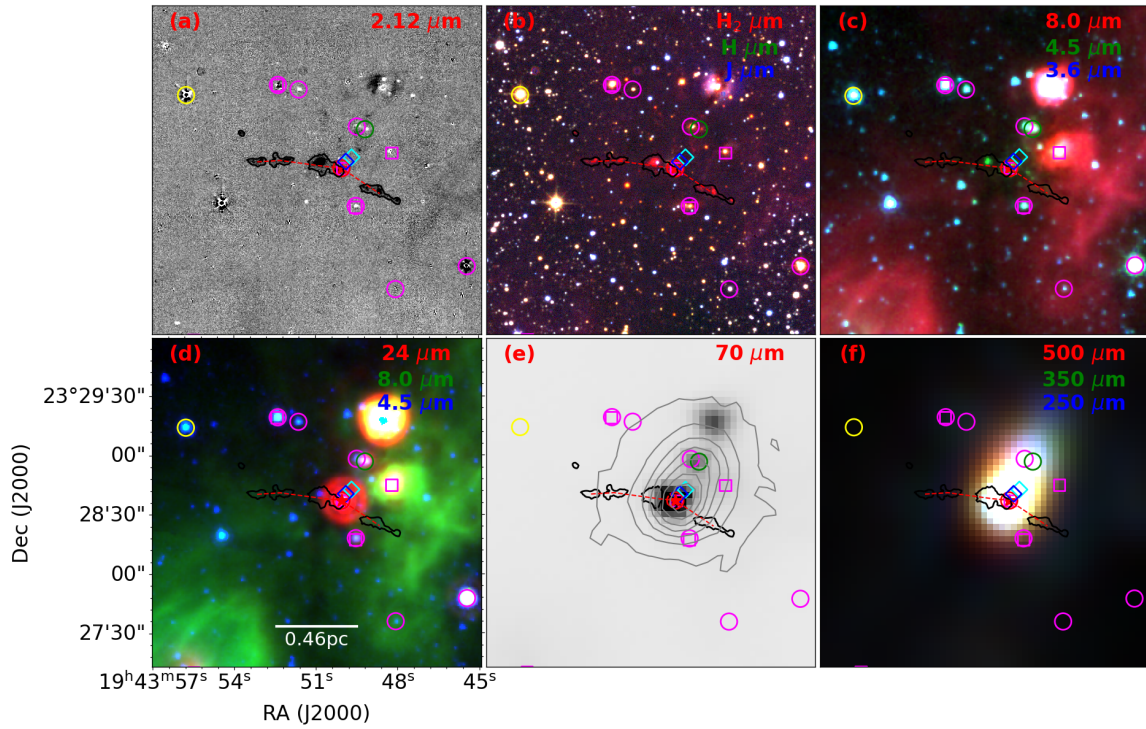


Figure 2. Colour-composite images for a curved outflow identified in the Vul OB1 complex. The image shown has the following layout: (a) Continuum-subtracted H₂-K image, (b) J (blue), H (green) and H₂ (red) colour-composite image, (c) IRAC 3.6 μm (blue), 4.5 μm (green) and 8.0 μm (red) colour-composite image, (d) IRAC 4.5 μm (blue), 8.0 μm (green) and MIPS 24 μm (red) colour-composite image, (e) PACS 70 μm image with ATLASGAL 870 μm contours shown in grey and (f) SPIRE 250 μm (blue), 350 μm (green), 500 μm (red) colour composite image. The knots identified in the F15 catalog are shown by black regions. YSOs identified in the field are denoted by the following symbols: red square box - PBR, magenta square box - YSO identified using 24 μm and 70 μm colour, red, magenta and orange circles - Class 0/I, II and II YSOs identified from [Billot et al. \(2010\)](#); [Kim et al. \(2015\)](#). The dashed red line connects all the knots linked to the outflow.

source candidates for outflows in this study, having both MIPS 24 μm and PACS 70 μm fluxes, satisfy the above-mentioned criterion. Protostars with extreme red colours satisfying $\log\left(\frac{\lambda F_{\lambda 70}}{\lambda F_{\lambda 24}}\right) > 1.65$ are identified as PACS Bright Red sources or PBRs. These large infrared excess sources are believed to be early-Class 0 sources ([Stutz et al. 2013](#)). In our study, we identify 2 PBRs based on their [24]-[70] colours.

Using the generated colour-composite images and the catalog of YSOs and likely protostars, we identify the driving source candidate(s) based on a careful visual inspection of the location of YSOs with respect to the MHOs. For MHOs consisting of single knots, a driving source candidate is assigned based on any prominent extension of the H₂ emission features and proximity to a nearby YSO. For MHOs with multiple driving sources in vicinity, driving source candidates are assigned based on jet alignment. In such cases, preference has also been given to sources with a SiO detection in the catalogue of [Csengeri et al. \(2016\)](#). We acknowledge the possible subjectivity in the above classification process. More detailed studies based on other shock tracers can be used to confirm the proposed associations (e.g. [Plunkett et al. 2013](#); [Zinchenko et al. 2015](#)). Table 1 shows the details of the outflows identified in this work and their physical parameters.

Based on the above approach, driving source candidates are identified for 79 (62%) outflows. Similar statistics is seen in other Galactic star-forming regions, where only 50-60% of the outflows were found to have associated driving sources (see [Samal et al. 2018](#), and references therein). Of the 79 outflows with identified driving sources, we find that 27 MHOs are bipolar in nature and 52 are unipolar. The

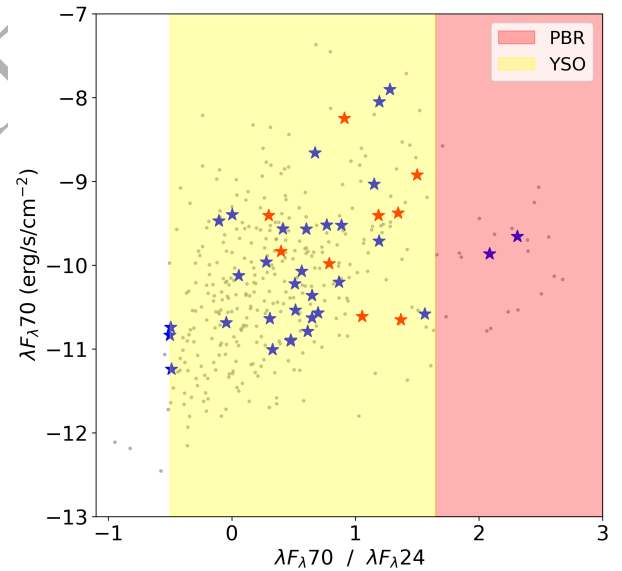


Figure 3. Plot of 70 μm flux as a function of the ratio of 70 μm to 24 μm flux. HOPS protostars ([Stutz et al. 2013](#); [Manoj et al. 2013](#)) are shown as grey dots. The blue stars are the YSOs identified in this study, having detection in IRAC bands. Deeply embedded sources lacking detection in the IRAC bands are plotted as red stars. The yellow shaded region corresponds to $\log\left(\frac{\lambda F_{\lambda 70}}{\lambda F_{\lambda 24}}\right) > -0.5$ which is used as the colour criterion for YSO identification. The red shaded regions represent PBRs, i.e., sources with $\log\left(\frac{\lambda F_{\lambda 70}}{\lambda F_{\lambda 24}}\right) > 1.65$.

Table 1. Sample table showing details of MHOs identified in Vul OB1 and IRDC G53.2

OF Name	MHO Name	R.A. ^a (J2000)	Dec ^a (J2000)	Cloud ^b	Source Name ^c	Morphology ^d	Lobe Length (pc) ^e	Lobe L _{2.12} (L _⊙) ^e
OF1	MHO 4218	19:41:44.0	23:14:12.0	Vul	G059.1854+00.1068	S-shaped, Bipolar	L: 0.18 R: 0.12	L: 0.001 R: 0.0009
OF2	MHO 4219	19:42:6.6	23:16:26.6	Vul	—	Linear, Unknown	—	—
OF3	MHO 4224	19:42:55.0	23:24:14.7	Vul	G059.4655-00.0457	Linear, Unipolar	1.8	0.0089
OF4	MHO 4216	19:41:1.2	22:3:9.9	Vul	G058.0750-00.3357	Single knot, Unipolar	0.8	0.002
OF5	MHO 4214	19:39:14.1	22:40:16.8	Vul	G058.4098+00.3279	Linear, Unipolar	0.35	0.004
OF6	MHO 2623	19:38:59.5	22:46:57.2	Vul	G058.4789+00.4318	Linear, Unipolar	1.19	0.0022
OF7	MHO 4210	19:38:37.3	22:41:16.5	Vul	—	Linear, Unknown	—	—
OF8	MHO 4208	19:38:33.3	22:43:5.0	Vul	J193833.26+224305.0	Linear, Unipolar	0.11	0.0052
OF9	MHO 4213	19:39:0.9	22:57:56.3	Vul	G058.6412+00.5168	Linear, Unipolar	0.07	0.0005
OF10	MHO 4209	19:38:36.5	23:4:43.8	Vul	—	Linear, Isolated knot	—	—

(a) For outflows without any driving source candidate, the location of the outflows are listed as the mean of the coordinates of the farthest knots. For isolated knots, the location of the outflow corresponds to the coordinates knot itself.

(b) Vul stands for Vulpecula OB association and IRDC is used to IRDC G53.2.

(c) The source names correspond to the name of the driving source candidates in the PSC of various Galactic plane surveys. Sources names with prefix 'G' indicate the coordinates of the point sources in GLIMPSE PSC (Spitzer Science 2009) in the Galactic coordinate system, 'MG' corresponds to sources from MIPS GAL PSC (Gutermuth & Heyer 2015). The prefix 'HIGALPB' and 'HIGALPR' indicates point sources from the Hi-GAL PSC (Molinari et al. 2016) in PACS 70 μ m and PACS 160 μ m bands, respectively. Source with prefix 'J' correspond to WISE PSC (Cutri & et al. 2012) and indicate the coordinates of the sources in equatorial system (J2000). The location of the outflows as listed in the table corresponds to the coordinates of the driving source candidate, if identified.

(d) This column lists the geometry and the nature of the outflow, i.e. unipolar, bipolar or multi-polar (more than one outflow).

(e) In case of bipolar outflows, 'L' is used to indicate properties of the left lobe and 'R' represents properties of right lobe.

Full table available in electronic version.

lower number of bipolar outflows identified could be attributed to high extinction which limits the detection of the red-shifted lobes in some cases. Additionally, other factors such as anisotropic ambient medium (e.g. Fernández-López et al. 2013) could lead to a higher unipolar outflow statistics compared to the bipolar counterparts as seen in this study.

3.2 Extinction and distance to identified MHOs

Extinction and distance information to individual MHOs is required in order to estimate the physical parameters. Extinction maps for the two clouds are generated using the PNICER algorithm developed by Meingast et al. (2017)⁹. Photometric data from the UKIDSS GPS point source catalog (Lucas et al. 2008) for the target area referred to as the science field here) and an extinction-free control field are provided as input to PNICER. The control field is identified as regions devoid of dust emission in the AKARI-FIR colour-composite images using Aladin sky atlas (Bonnarel et al. 2000). PNICER calculates the colour excess for point sources in the science field using the colours of stars inside the control field and returns a discrete extinction map at K-band. Subsequently, the maps are smoothed to a resolution of 30'' with pixel scale of 15'' (i.e. 0.12 pc and 0.17 pc corresponding to a distance of 1.7 and 2.3 kpc, respectively). The generated extinction maps are presented in Figure 4a and 4b for Vul OB1 and IRDC G53.2, respectively. Since the pixel scale is much larger than the typical size of H₂ knots, we use the value of the pixel corresponding to the knot as our estimate of extinction. Few regions of high extinction and hence with smaller stellar densities compared to our control field appear as dark patches in the extinction map. For such cases, we use a lower resolution 1' and pixel scale of 30'' extinction map. We note, due to beam dilution, the extinction values in dense compact regions are likely to be underestimated.

⁹ <http://smeingast.github.io/PNICER/>

CO velocity-integrated contours, generated using CO data cubes from Dame et al. (2001); Jackson et al. (2006), are overlaid in Figure 4a and 4b. The contours represent emissions between cloud velocity ranges of $v = 20-40$ km s⁻¹ and $v = 15-30$ km s⁻¹ taken from Billot et al. (2010) and Kim et al. (2015) for the Vul OB1 and IRDC G53.2 complexes, respectively. The outermost contours, corresponding to the 3 σ levels, define approximate boundaries for the complexes. MHOs lying within and close to the 3 σ emissions are considered to be associated with the parent cloud complex. In the absence of distance information for individual outflows, we assume a common distance for all outflows within the same cloud complex. As seen in Figure 4, the majority of the detected MHOs lie within the cloud boundaries defined by the 3 σ levels, with some exceptions in the IRDC G53.2. While the MHOs lying outside the cloud boundaries from CO maps may still be part of the cloud, they have been excluded from further analysis.

It should be kept in mind that physical association of individual MHOs is difficult to confirm from this plane-of-sky correlation, as it is not possible to distinguish MHOs driven by foreground/background YSOs. Based on the CO data, we find no other major cloud components along the line-of-sight of both the complexes. Hence, we assume that the contamination from other Galactic MHOs would be minimal in our identified sample.

3.3 Outflow lobe length and H₂ 1-0S(1) line-luminosity distribution

Following the approach of Makin & Froebrich (2018), we consider individual outflow lobes irrespective of bipolar or unipolar outflow identification for estimating the lobe length. It should be noted that these estimates for outflow lobe length have not been corrected for inclination and thus should be treated as lower limits. Figure 5a shows the number distribution of the lobe length estimates. The distribution yields a consistently larger median lobe length of 0.22 pc for Vul OB1 as compared to 0.17 pc for IRDC G53.2. In comparison, they

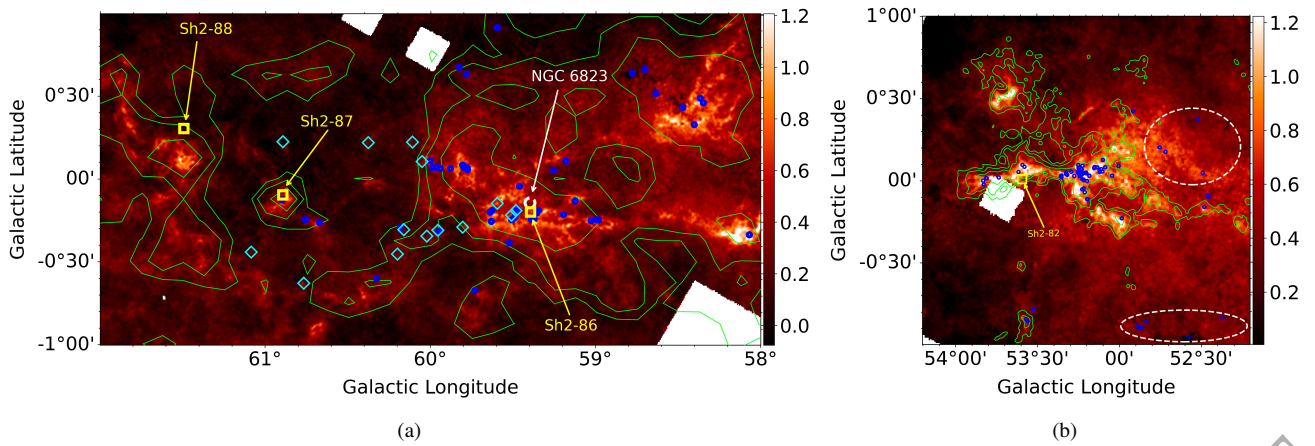


Figure 4. Extinction map for (a) Vul OB1 and (b) IRDC G53.2 generated using PNICER with a resolution of 1'. The blue dots show the locations of the MHOs identified using the continuum-subtracted images and the green contours represent the 3σ , 5σ and 10σ boundaries from the CO velocity-integrated map from Dame et al. (2001) and Jackson et al. (2006). The location of various pillars in Vul OB identified by Billot et al. (2010) are shown by cyan diamonds. HII regions from Sharpless (1959) are depicted by yellow box. The white dashed regions in (b) show the MHOs outside the boundary of IRDC G53.2. The empty square corresponds to regions lacking data in the GPS survey.

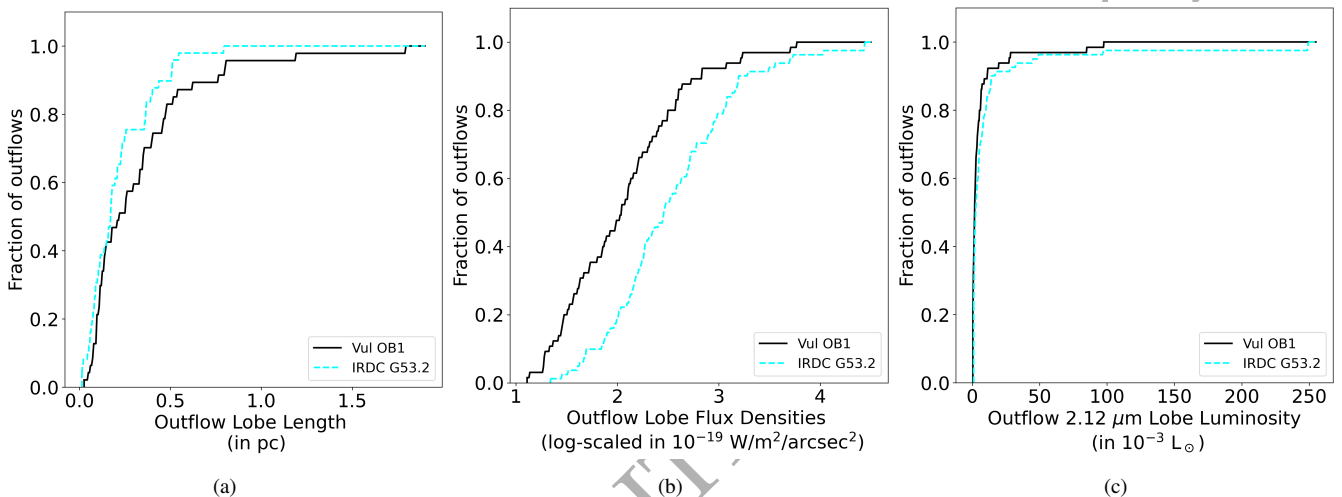


Figure 5. Cumulative distribution function of (a) outflow lobe length, (b) outflow lobe H_2 1-0S(1) flux density and (c) H_2 1-0S(1) line-luminosity of outflow lobes in Vul OB1 and IRDC G53.2.

are similar in angular units (~ 20 arcsec), thus indicating the effect of distance on the physical lengths. The observed lobe lengths are consistent with the range of $\sim 0.2 - 0.4$ pc seen in other complexes like Aquila, Orion A, Cassiopeia and Auriga, Serpens and Aquila, Cygnus-X and M17 (Zhang et al. 2013; Stanke et al. 2002; Ioannidis & Froebrich 2012a; Froebrich & Makin 2016; Makin & Froebrich 2018; Samal et al. 2018).

From observations of several clouds, it is seen that long, parsec-scale outflows are few (Davis et al. 2009; Ioannidis & Froebrich 2012a; Stanke et al. 2002; Makin & Froebrich 2018). Considering both complexes, around 10% of the outflow lobes with known driving source candidates are estimated to be longer than 0.5 pc and 7 outflows have a total length greater than 1 pc. However, the actual number of parsec-scaled outflows may be higher if corrected for the effect of outflow inclination. Furthermore, the H_2 1-0S(1) line traces only the hot and dense region of the outflows and has a fast cooling rate. Thus, some of the evolved and faint emission features might lack detection, especially at large distances. Sensitive optical obser-

vations in the H_α and [SII] lines are required to trace distant outflows in low density regions of the cloud.

The flux densities of each H_2 emission knot are retrieved from the F15 catalog. The retrieved flux densities are then de-reddened using the following expression

$$F_{\text{dered}} = F_0 \times 10^{\frac{A_{2.12\mu\text{m}}}{2.5}} \quad (1)$$

where F_{dered} is the de-reddened knot flux, F_0 is the knot flux at $2.12 \mu\text{m}$ and $A_{2.12\mu\text{m}}$ is the extinction value at $2.12 \mu\text{m}$ calculated using the A_K value from the extinction map ($A_{2.12} = 1.06 \times A_K$ from Cardelli et al. 1989). Subsequently, the H_2 1-0S(1) line flux density and luminosity of the identified lobes are calculated. For a typical jet/outflow temperature of 2200 K, the H_2 1-0S(1) line luminosity accounts for roughly one-twelfth the total H_2 luminosity emitted from shock-excited H_2 (Caratti o Garatti et al. 2006).

Figure 5b and 5c show the distribution of the outflow lobe flux densities and the lobe H_2 line-luminosity, respectively. The outflow lobe flux densities vary between 1.2×10^{-18} to $2.7 \times$

$10^{-15} \text{ W/m}^2/\text{arcsec}^2$ with median value of $1.1 \times 10^{-17} \text{ W/m}^2/\text{arcsec}^2$ and $2.9 \times 10^{-17} \text{ W/m}^2/\text{arcsec}^2$ for Vul OB1 and IRDC G53.2 respectively.

It should be noted that, the flux density of the faintest H_2 knot identified in this study ($5.9 \times 10^{-19} \text{ W/m}^2/\text{arcsec}^2$) is comparable to the detection limit of H_2 features in surveys of nearby clouds ($1 - 7 \times 10^{-19} \text{ W/m}^2/\text{arcsec}^2$ in Stanke et al. 2002; Zhang et al. 2015; Davis et al. 2009; Zhang et al. 2013). However, since sources in our study are located significantly farther away, the faintest outflow identified in this study is nearly 17 times more luminous than the faintest outflow in Orion A (Stanke et al. 2002) and 233 times more brighter compared to the faintest outflow in Aquila molecular cloud (Zhang et al. 2015). These differences suggest a possible bias towards more luminous outflows from intermediate- and high-mass stars in our study.

3.4 Distribution of YSO mass and luminosity from SED models

Li et al. (2018) show that the mechanical force of outflows from protostars is well correlated with the bolometric luminosity of the central source and the correlation holds good over the entire mass regime. The bolometric luminosity of protostars is mainly dominated by energy release associated with accretion of matter. However, for late stage YSOs, the photometric luminosity dominates the accretion luminosity. In order to obtain reliable estimates of photometric luminosity of the driving source candidates, we use the SED-fitting tool¹⁰ developed by Robitaille (2017, hereafter R17). The SED-fitter uses χ^2 -minimization to fit the observed SEDs of YSOs to a large grid of YSO model SEDs spanning a large parameter space for physical properties like dust distribution, radius and temperature of central star, etc. The R17 model addresses some of the caveats of the SED models from Robitaille et al. (2006, hereafter R06) by eliminating highly model-dependent parameters which do not directly affect the SEDs, such as mass, luminosity and envelope infall rates. The R17 models also provide a wider and uniformly distributed parameters compared to the R06 models. The R17 models comprise of 18 different models of varying complexities with different combinations of YSO parameters, offering modularity to the users in choosing the model that best represent the source parameters. These models are named using characters representing presence of different components in the model, for instance, the model ‘spubhmi’ corresponds to a source with a central star (s) with a passive disk (p), ulrich envelope (u), bipolar cavities (b), inner hole (h), ambient medium (m) and interstellar dust (i) (refer to R17 for a detailed description of all 18 models).

Photometric data, covering the wavelength range of 1.2–70 μm , taken from UKIDSS-GPS, GLIMPSE, MIPS GAL, and Hi-GAL catalogs (Spitzer Science 2009; Gutermuth & Heyer 2015; Lucas et al. 2008; Molinari et al. 2016) are provided as inputs to the SED-fitting tool. Based on distance estimates from literature (Billot et al. 2010; Kim et al. 2015) and keeping in mind the uncertainties associated with these values, we use a conservative distance range of 2.0 to 2.5 kpc for Vul OB1 and 1.5 to 2.0 kpc for IRDC G53.2 for the SED modelling. Visual extinction input is allowed to vary from 2 to 50 mag. Taking 1 mag per kpc increase in A_V (Stahler & Palla 2004) sets the lower limit of the foreground extinction in the direction of both the clouds, while the typical maximum extinction seen towards extended green objects (EGOs) or ‘green fuzzies’ (Cyganowski et al.

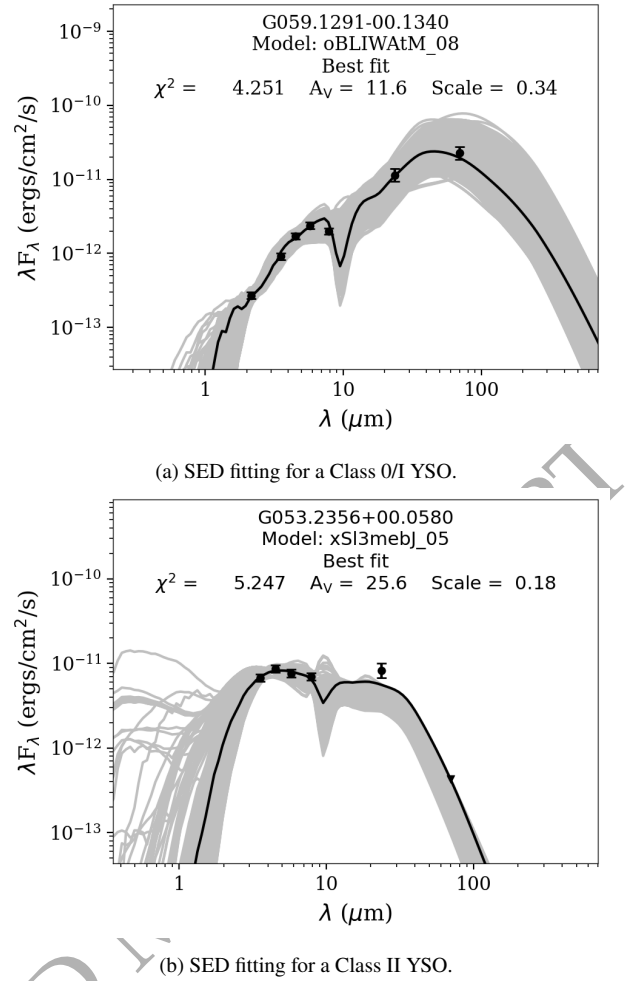


Figure 6. Sample output from SED fitting using R17 models showing the good-fit models that satisfy the $\chi^2 - \chi^2_{\min} \leq 9N_{\text{data}}$ criteria. The black dots are the observed photometric data points given as input. The black SED corresponds to the best-fit model, and the gray SEDs are for the remaining models that are consistent with the input fluxes. It should be noted that χ^2_{\min} represents the least χ^2 for the source across all 18 SED models.

2008, EGOs) and Ultracompact HII regions (UCHII, Hanson et al. 2002; Caratti o Garatti et al. 2015) is taken as the upper limit.

Longer wavelength (24 and 70 μm) flux densities are important for constraining the fitted SED models (Dunham et al. 2006). For undetected and saturated sources in these bands, we use the faintest and brightest flux densities from the point source catalog (see Section 2) and use them as upper and lower limits, respectively. Similar to Samal et al. (2018), we use a conservative 10% uncertainty on the flux density values of UKIDSS and GLIMPSE surveys and 20% uncertainty on MIPS GAL and Hi-GAL flux density measurements. In order to avoid any bias, we follow the approach described in the R17 paper. For every YSO, SED-fitting is carried for all 18 models and the minimum χ^2 value (χ^2_{\min}) for the best-fit model across all 18 models is determined. A relative score for each model is generated based on the likelihood of the model ($P(D|M)$ = fraction of good-fit SEDs identified relative to the total number of SEDs in the model) to provide a fit to the input flux densities with a broadened threshold of $\chi^2 - \chi^2_{\min} \leq 9N_{\text{data}}$. Here, N_{data} is the number of photometric data points used. Sample SEDs and the fitted models for a Class 0/I and a Class II YSO are shown in Figure 6. The physical

¹⁰ <https://sedfitter.readthedocs.io/en/stable/>

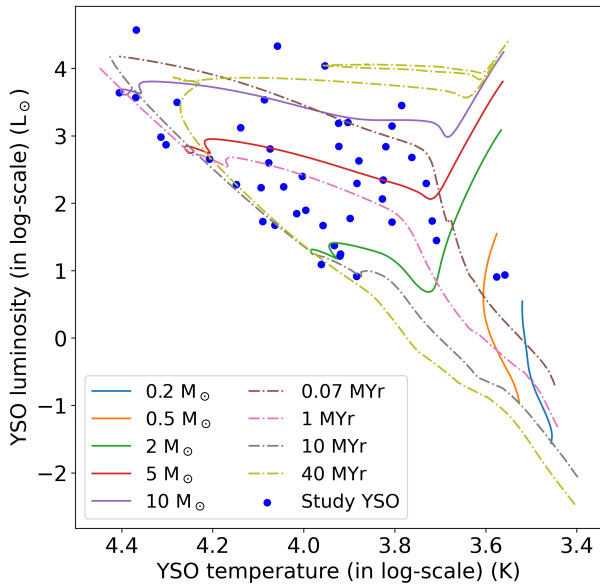
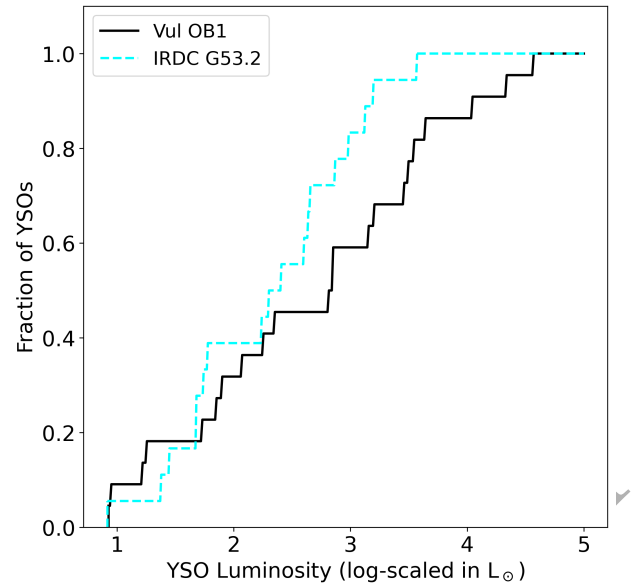


Figure 7. HR diagram of driving source candidates for MHOs identified in this study. Solid lines represent the evolutionary track of sources with the same mass and dashed lines represent the isochrone tracks. The blue dots represent the driving source candidates identified in this study.

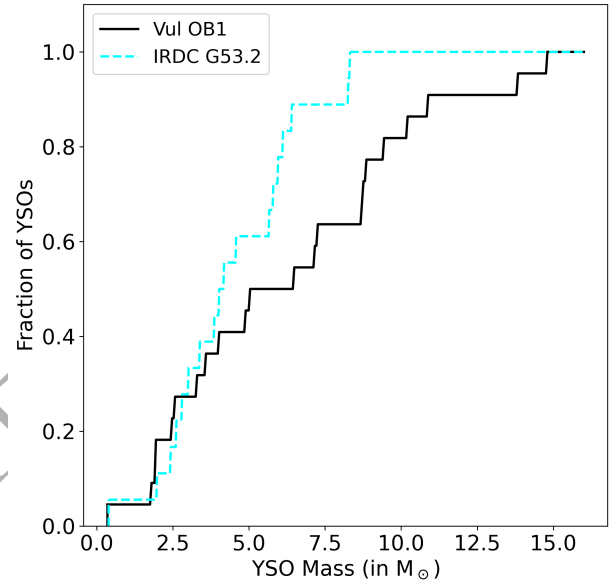
parameters of each source are determined by using the model with the highest score. Exponential weights ($e^{-\frac{\chi^2}{2}}$) are assigned to the retrieved parameters of the chosen model, such that model fits with lower χ^2 values are given a higher weight. The weighted mean and the corresponding error (standard deviation) of the model-derived physical parameters are listed in Table. 2. Since the R17 models returns only the temperature and radius of the YSO as parameters of the central source, we used the Stephen-Boltzmann law to estimate the photometric luminosity of the YSOs.

For estimating the mass of the sources, we use the Parsec Isochrone Datasets (Bressan et al. 2012) of solar metallicity and mass corresponding to the closest evolutionary track in the HR diagram is used as the mass of the YSO. Figure 7 shows the HR diagram for the identified driving source candidates. We note that stellar parameters of YSOs are better constrained by SED models when optical measurements are available, which is not the case for the YSOs in our sample. Hence, these estimated values should be considered as indicative only. Additional high-sensitivity optical and infrared photometric observations are needed to accurately measure the stellar properties of the sources. Moreover, young pre-main-sequence (PMS) stars, in particular those associated with jets/outflows, are highly variable. Variability can induce enormous changes in their position in the HR diagram. In the present work, we reject those sources that lie significantly outwards of the boundaries defined by the HR diagram. In the case of high to intermediate stars, since PMS evolutionary track of a given mass star is nearly horizontal for different ages, thus, effect of uncertainty in age has less impact on the mass estimation.

The cumulative distribution functions of the mass and luminosity of the 45 selected driving source candidates are shown in Figure 8. The estimated mass and luminosity of the driving source candidates range between ~ 0.1 - $15 M_{\odot}$ and ~ 2 - $37226 L_{\odot}$, respectively. The median values of the derived mass and luminosity are $\sim 4.4 M_{\odot}$ and $\sim 221 L_{\odot}$, respectively. While 10 sources are candidate massive YSOs ($> 8 M_{\odot}$), the median value suggests that the majority of the



(a)



(b)

Figure 8. Cumulative distribution function of (a) luminosity and (b) mass of driving source candidates in Vul OB1 and IRDC G53.2.

outflows identified in this work are likely driven by intermediate mass stars. From SED-fitting, we find that majority of the YSOs have an inclination angle of 40-50 degrees relative to the plane of the sky. Assuming a typical inclination angle of 45 degrees, our estimate of outflow lobe lengths could be under-estimated by a factor of only ~ 1.4 .

4 DISCUSSION

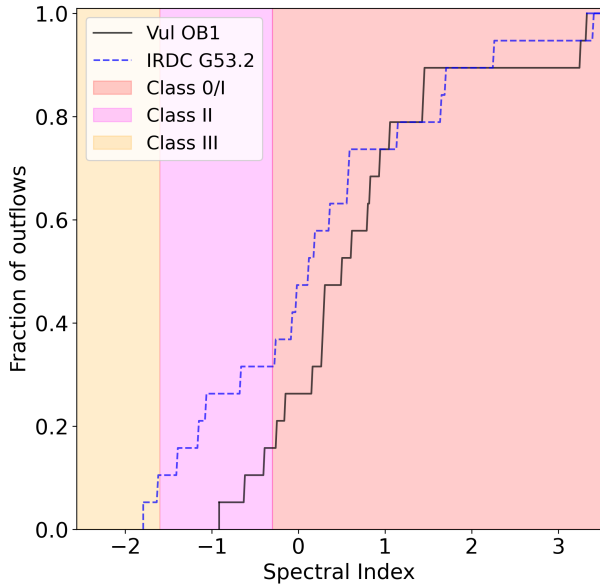
4.1 Dominant evolutionary class for jet-bearing YSOs

In both complexes, the identified YSOs have been classified using various photometric criteria in literature (Billot et al. 2010; Kim et al. 2015). However, for uniformity, we classify the identified driving

Table 2. Sample table showing details of physical properties of driving source candidates of MHOs identified in Vul OB1 and IRDC G53.2

OF Name	MHO Name	Source Name	YSO temperature (K)	YSO luminosity (L_{\odot})	YSO mass (M_{\odot})
OF1	MHO 4218	G059.1854+00.1068	11079±3926	176±102	3.6
OF2	MHO 4219	—	—	—	—
OF3	MHO 4224	G059.4655-00.0457	12208±5861	3441±2757	8.8
OF4	MHO 4216	G058.0750-00.3357	6607±4185	693±596	7.2
OF5	MHO 4214	G058.4098+00.3279	7997±6690	1587±1097	8.7
OF6	MHO 2623	G058.4789+00.4318	6685±291	222±31	5.0
OF7	MHO 4210	—	—	—	—
OF8	MHO 4208	J193833.26+224305.0	—	—	—
OF9	MHO 4213	G058.6412+00.5168	—	—	—
OF10	MHO 4209	—	—	—	—

Full table available in electronic version.

**Figure 9.** Cumulative distribution function of spectral index (α) of driving source candidates for outflows in Vul OB1 and IRDC G53.2

source candidate YSOs based on the infrared spectral index, $\alpha_{\text{IR}} = d\log(\lambda F_{\lambda})/d\log(\lambda)$ (Lada 1987). α is estimated as the slope of the SED of the YSOs using the IRAC bands (3.6–8.0 μm). Following Greene et al. (1994) and Billot et al. (2010), we classify the YSOs, as Class 0/I ($\alpha_{\text{IRAC}} > -0.3$), Class II ($-1.6 < \alpha_{\text{IRAC}} < -0.3$) and Class III YSOs ($-2.56 < \alpha_{\text{IRAC}} < -1.6$).

Figure 9 shows the cumulative distribution function of the jet-bearing YSOs as a function of the estimated spectral index values. The plot shows that approximately 79% of the driving source candidates for the identified outflows are Class 0/I sources, 17% are Class II YSOs and 4% are Class III YSOs. The distribution obtained is consistent with the fact that H_2 jets are believed to be most prominent in the early Class 0/I stage and the outflow activity fades away as the YSO evolves. This corroborates with the hydro-dynamical simulations of Vorobyov & Basu (2015), who show that episodic accretion events, induced by gravitational instabilities, and disk fragmentation are present mostly during the early evolutionary stages of a protostar.

It should be noted that there could be an inherent observational bias towards embedded Class 0/I YSOs in our study. Due to the molecular gas and dust envelope surrounding Class 0/I YSOs, MHOs are more prominent for early stage protostars. However, outflows from evolved

YSOs may not be detected as MHOs since their immediate environment would have less molecular gas. Sensitive optical observations in $\text{H}\alpha$ and [SII] bands are hence essential to get a better insight into this observed trend.

4.2 H_2 emission knots in outflows

Chains of H_2 emission knots associated to a jet/outflow are indicative of the fact that the driving YSO has undergone episodic ejection (e.g. Bachiller 1996), likely due to underlying variability in the mass accretion (Scholz et al. 2013; Machida & Basu 2019; Takami et al. 2020). These accretion bursts could originate from disk-instability in the early evolutionary phases of the YSOs (Zakri et al. 2022).

It is believed that accretion processes, that include both the declining accretion rates and episodic accretion outbursts, could resolve the luminosity problem of protostars (Dunham et al. 2012; Herczeg et al. 2017, and references therein). Several H_2 surveys, using the UWISH2 database, have observed typical ejection timescales of few kyr (e.g. Ioannidis & Froebrich 2012b; Froebrich & Makin 2016; Makin & Froebrich 2018) suggesting an intermediate eruption timescale, between the well-known FU-Ori and EX-Ori type eruptions in low-mass YSOs. The origin of these eruptions, characterised by moderate to large increase in the brightness of the source, is still debated (Audard et al. 2014; Hales et al. 2020; Szegedi-Elek et al. 2020). Brightening ~ 5 magnitudes in the V band is seen in FU-Ori types (Hartmann & Kenyon 1985) as compared to 2–4 magnitudes increase in EX-Ori type eruptions (Hales et al. 2020). Detailed studies on these periodic ejections can enable a better understanding of the mechanisms involved and help in constraining YSO models.

The separation between subsequent H_2 emission knots is thus a useful parameter to be determined. This will enable understanding the periodicity in ejection of jets and the possible origin of enhanced accretion in YSOs. These gaps are measured as the separation of mean locations of adjacent H_2 knots seen in the continuum-subtracted images. The distribution of knot gaps for MHOs in our study is plotted in Figure 10 showing a peak at 0.1 pc. Using a transversal velocity of 80 kms^{-1} , the typical velocity used in similar studies based on the UWISH2 survey (e.g., Ioannidis & Froebrich 2012b), the knots are found to be separated by ~ 1.2 kyr in time for outflows, similar to the timescales observed by Makin & Froebrich (2018). Since the majority of the outflows in this study are driven by Class 0/I YSOs, these timescales are consistent with the estimated burst intervals of ~ 1000 yr for early embedded protostars from the *Spitzer* and WISE epochs separated by 6.5 yr (see Fischer et al. 2019). This also corroborates with the recent findings of Park et al. (2021),

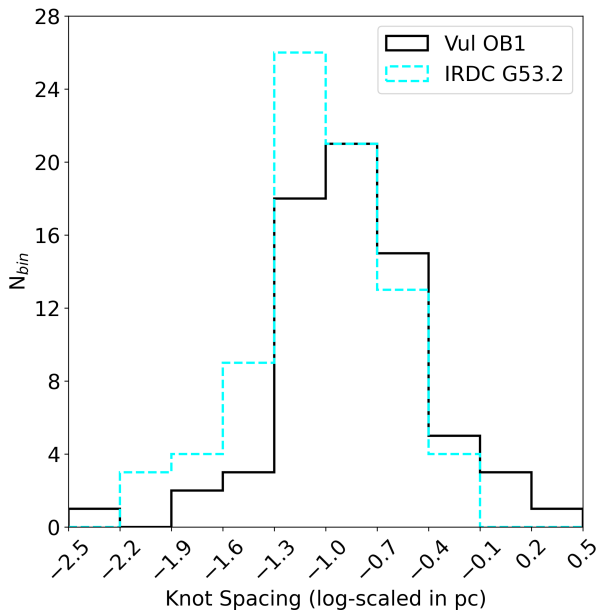


Figure 10. Distribution of knot gaps (in log-scale) for outflows in Vul OB1 and IRDC G53.2.

who suggest that YSOs in earlier evolutionary stages have higher amplitudes of variability with recurrence timescale of ~ 1000 yr.

The estimated timescale of the majority of the outflows in Vul OB1 and IRDC G53.2 lies in between the range of 5-50 kyr for FU-Ori (Scholz et al. 2013) and 1-10 yr for EX-Ori (Aspin et al. 2010) type of eruptions. The observed timescales also lie in between the bi-modal distribution for the outburst timescales observed by Vorobyov et al. (2018) for isolated and clustered luminosity bursts. This implies that we are probably witnessing ejecta from an intermediate class of eruptive variables similar to MNors (Contreras Peña et al. 2017, 2019). More detailed models are required to understand these intermediate eruption timescales and to establish a robust link between the accretion and ejection process based on the observed variability (Nony et al. 2020).

4.3 Observed correlation between outflow and driving source parameters

Using the various physical parameters estimated for the outflows and the driving source candidates, we examine the parameter space for trends and correlations, if present. Figure 11 represents variation of the outflow lobe length with lobe flux densities. The correlation seen, although weak, indicates that longer outflows are also typically brighter. The figure also plots data from Makin & Froebrich (2018) and the corresponding 3σ interval identified from linear regression between outflow lobe length and flux densities. As seen, the derived parameters of the majority of the outflows identified in Vul OB1 and IRDC G53.2 are consistent with results from the above mentioned study.

A scatter plot of the lobe length of MHOs and the estimated spectral index is shown in Figure 12. No correlation between these parameters is evident similar to the findings of Davis et al. (2009); Zhang et al. (2015). Inaccurate parameter estimates from H_2 observations (e.g. effect of extinction and inclination on lobe length), variation of spectral indices due to variability and confusion with the nearby sources, could affect any correlation, if present. Moreover,

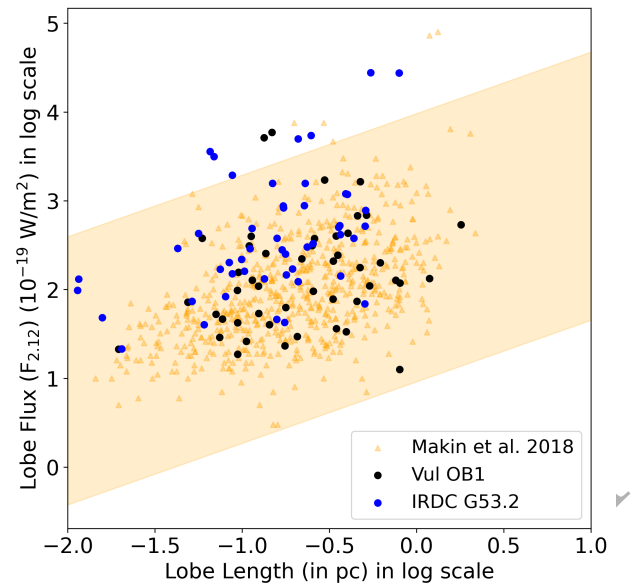


Figure 11. Variation of length of outflows identified in Vul OB1 and IRDC G53.2 with the H_2 1-0S(1) line flux densities. The black dots corresponds to outflows identified in Vul OB1, blue dots for IRDC G53.2 and the orange triangles denote outflows from Makin & Froebrich (2018). The orange shaded region shows the 3σ interval identified using linear regression for outflows from Makin & Froebrich (2018).

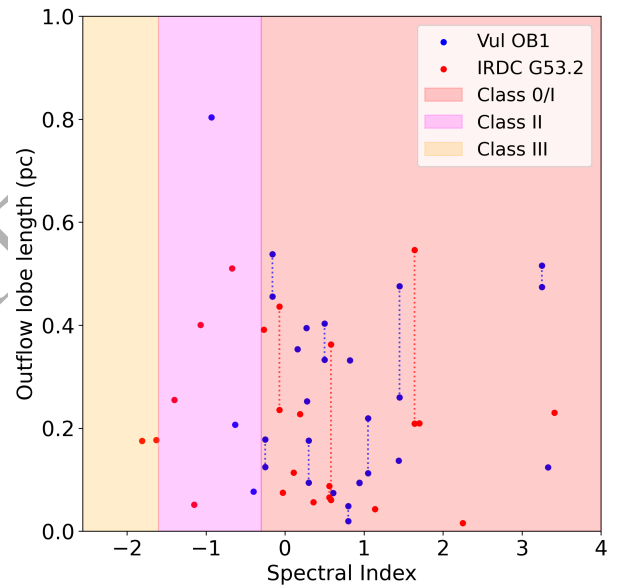


Figure 12. Variation of outflow lobe length with spectral index. The blue and red dots correspond to MHOs in Vul OB1 and IRDC G53.2 respectively. Outflow lobes corresponding to bipolar MHOs are connected using dotted vertical lines.

lobe lengths are expected to be short at the starting phase of ejection by a YSO. Similarly, jets are expected to fade, thus are more difficult to observe, in the late phase of a YSO with declining accretion.

In Figure 13, we show the total H_2 luminosity of outflows as a function of the photometric luminosity of the corresponding driving source candidates. The figure also shows data points from Caratti o Garatti et al. (2006, 2015). In agreement with the findings of Caratti o Garatti et al. (2006, 2015), we observe that MHOs with higher H_2

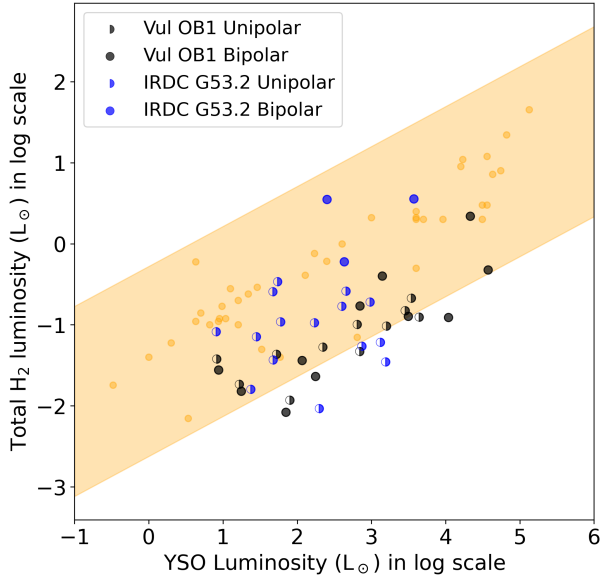


Figure 13. H_2 luminosity of the outflows vs photometric luminosity of the driving source candidate. The orange data points are from Caratti o Garatti et al. (2006, 2015) and the corresponding 3σ interval is shown by the orange shaded region. All the parameters are in logarithmic scale. The black data points are from Vul OB1 and blue data points are from IRDC G53.2. Bipolar outflows are shown by filled circles, and the half-filled circles represent unipolar flows.

luminosities are driven by more luminous YSOs in our study region. However, we note that the sources in our study deviate from the 3σ interval of Caratti o Garatti et al. (2006, 2015). This deviation could arise from an under-estimation of the H_2 luminosities of the outflows as even an uncertainty of 1 magnitude in A_V could affect the estimated $L_{2.12}$ by 10% (see Caratti o Garatti et al. 2006). Unlike sources from Caratti o Garatti et al. (2006, 2015), who have used near-IR spectral line observations to calculate the temperature and extinction, we use a low-resolution extinction map for extinction correction and 2000K as the temperature of the shocked jets. Alternatively, the deviation in the figure could also indicate an over-estimation of luminosity of driving source candidates in our study. Such deviation may be due to lower spatial resolution measurements at longer wavelengths. High resolution mid- and far-infrared observations would be needed to better understand the observed deviation.

Although the correlations observed are not strong, the trends observed pave the way for more detailed studies and confirm the existence of a link between the physical properties of outflows and their driving source candidates. Despite the scatter, these results provide limits on the estimates of various physical properties of both the outflows and the YSOs. These findings paired with high resolution observations can help with our understanding of the origin and dynamics of outflows and YSOs.

5 NOTES ON INDIVIDUAL OUTFLOWS

In this work, we have identified 127 jets/outflows displaying interesting morphology and properties. Of the identified outflows, 2 are likely quadrupolar (OF56/MHO2647 and OF57/MHO2646, OF104/MHO2640 and OF105/MHO2641), 2 are associated with dark clouds (OF39/MHO4233 and OF42/MHO4238), 3 outflows show bent or curved morphology (OF1/MHO4218,

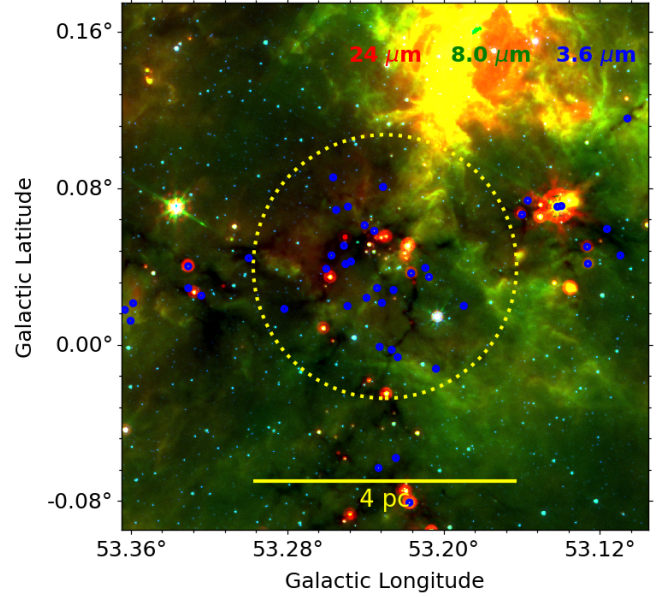


Figure 14. Multi-wavelength color-composite of a hub-filament system in IRDC G53.2 (IRAC 3.6 μm as blue, 8.0 μm as green and MIPS 24 μm as red). MHOs identified in this study are shown by blue dots. The yellow dotted circle indicates the central region of the hub-filament system.

OF20/MHO4235 and OF33/MHO4244), and 2 are located inside pillars (OF35/MHO4234 and OF37/MHO4249). We find enhanced green emission in the IRAC colour-composite images for 6 outflows implying that they could possibly belong to the population of EGOs. Brief discussion on some of these interesting outflows are given here and discussion on the rest are available in the electronic version.

A protocluster with cluster of jets in IRDC G53.2

Figure 14 shows the IRAC color-composite of an active star forming region ($l \sim 53.23^\circ$, $b \sim 0.04^\circ$) within the IRDC G53.2. We observe a clustering of YSOs in a central region with a radius of 2 pc. In the infrared, the region appears to be dark, while from Wang et al. (2020) we find that it corresponds to a clumpy structure with enhanced emission in dense gas tracers such as HCN, HCO^+ and N_2H^+ . The region also corresponds to an embedded cluster, "G3CC 70", detected in the *Spitzer*-GLIMPSE survey by Morales et al. (2013). Thus, it is an ideal candidate for studying the role of protostellar feedback on the formation and growth of star clusters (e.g. Murray et al. 2018; Rosen & Krumholz 2020; Verliat et al. 2022) using high-resolution molecular observations (e.g. Maury et al. 2009; Nakamura et al. 2011; Baug et al. 2021).

OF33/MHO4244

Figure 2 shows multi-band colour composite image of a curved outflow identified in the Vul OB1. The C-shaped geometry depicting the curvature of the outflow can arise from the motion of the surrounding ambient medium with respect to the outflow or from proper motion of the YSO itself (Bally et al. 2007; Cunningham et al. 2009; Reipurth & Bally 2001). Similarly, S-shaped geometries have also been found in literature (e.g. see HH 315 in Reipurth et al. 1997), which suggests a precessing jet likely due to the presence of a companion to the outflow driving source.

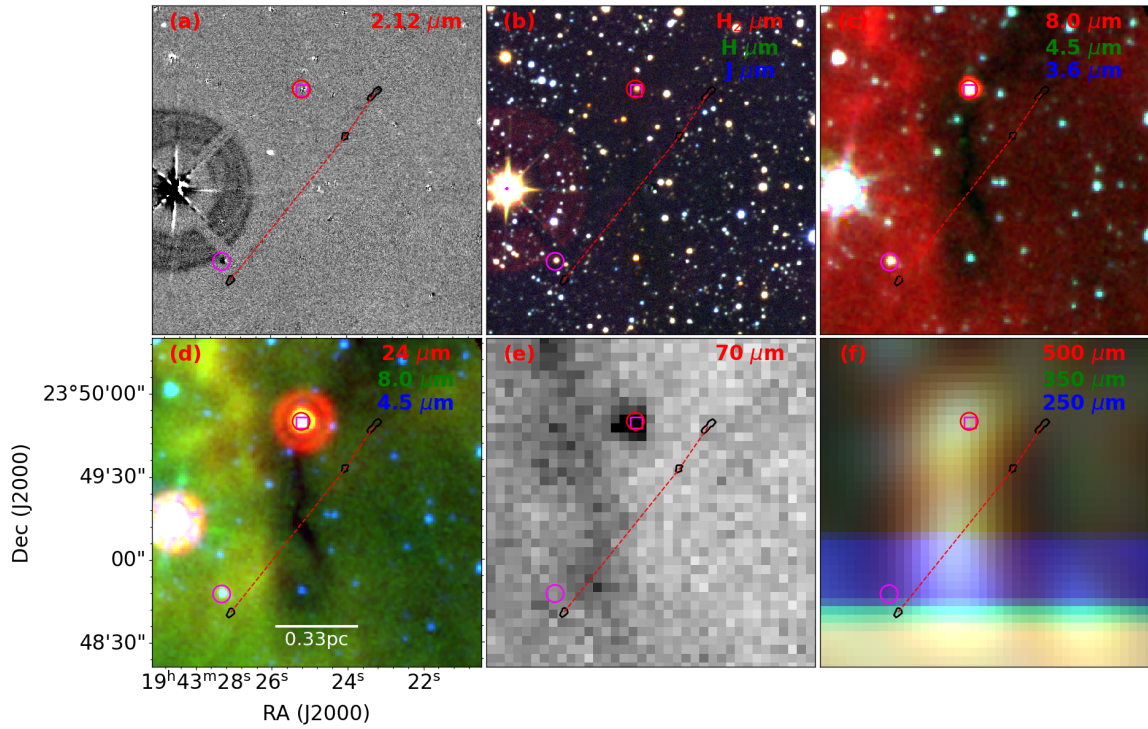


Figure 15. Multi-band image of outflow OF39/MHO4233 originating from a dark cloud. The layout, colours and symbols are the same as Figure 2.

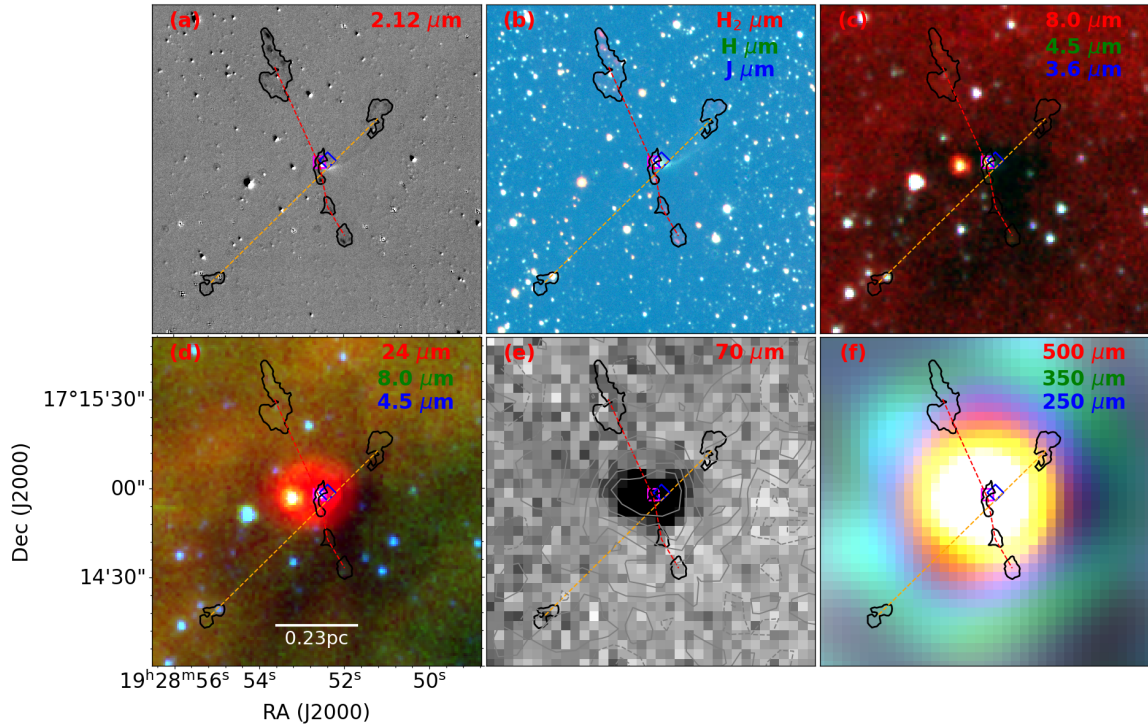


Figure 16. Multi-band image of a quadrupolar outflow OF104/MHO2640, OF105/MHO2641 in IRDC G53.2. The two outflows are shown by red and orange dashed lines. The figure follows the same layout, colours and symbols as Figure 2

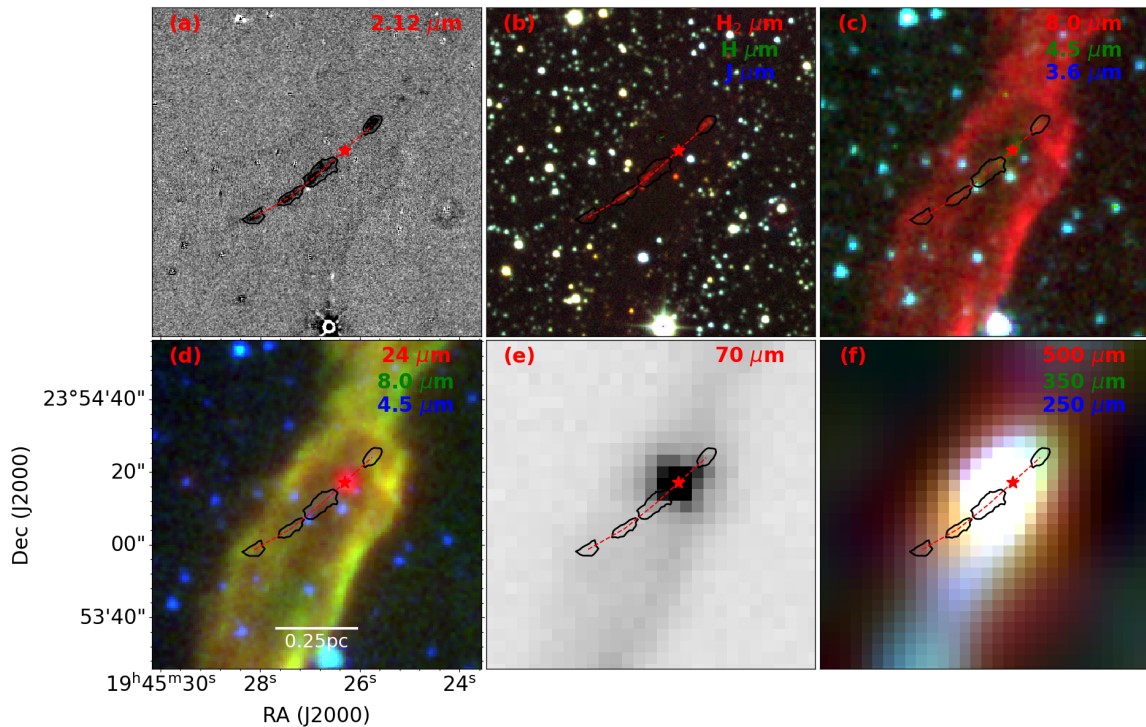


Figure 17. Multi-band image of outflow OF37/MHO4249 inside a pillar in Vul OB1. The layout, colours and symbols are the same as given in Figure 2.

OF39/MHO4233

Figure 15 shows multi-band colour-composite images of the identified outflow OF39/MHO4233 in the Vul OB1 complex and the region associated with it. The figure displays an interesting case of an outflow likely originating from a deeply embedded YSO inside the dark cloud. No driving source is identifiable up to $70 \mu\text{m}$. The outflow is observed to be oriented away from the axis of the filamentary dark cloud. Such alignments between outflows and filaments could be a result of continuous transport of mass from the filament onto the protostellar core in the presence of moderately strong magnetic field lines (e.g. Kong et al. 2019, and reference therein). These deeply embedded candidates are ideal targets to study the earliest stages of protostellar evolution.

OF104/MHO2640 and OF105/MHO2641

In Figure 16, we show the multi-band images of a likely quadrupolar outflow, OF104/MHO2640 and OF105/MHO2641, identified in the IRDC G53.2 comprised of two bipolar outflows. The driving source candidates responsible for the two outflows are not resolved in the images presented. Better sensitivity and higher resolution images are required to detect the YSOs responsible for individual outflows. Similar multi-polar outflows, such as HH 124 and HH 571/572 from NGC 2264N and HH 111, have been observed and are of great importance as they could be potential indicators of binary star formation (Reipurth et al. 1999, 2004; Makin & Froebrich 2018; Wolf-Chase et al. 2017).

OF37/MHO4249

We discover an interesting case of an outflow, OF37/MHO4249, inside one of the pillars in Vul OB1 (named VulP1 in Billot et al.

2010). The corresponding multi-band images for this 0.5 pc long outflow are shown in Figure 17. The driving source candidate of the outflow is a PBR implying an early Class-0 object. Though enhanced green emission is discernible, the source has not been identified in existing catalogs of EGOs (Cyganowski et al. 2008; Chambers et al. 2009). The luminosity of the source is estimated to be $\sim 75 L_{\odot}$ using the correlation between the $70 \mu\text{m}$ flux and bolometric luminosity of protostars as observed by Dunham et al. (2008) as the source lacked sufficient data points for SED-fitting. This outflow presents itself as an excellent site of triggered star formation and is an ideal target for follow-up studies. Another case of triggered star formation inside a pillar has been discussed in the online material (see OF35/MHO4234).

6 CONCLUSIONS

We present the result of a statistical analysis of jet bearing YSOs in two interesting star forming complexes, the Vul OB1 association and the IRDC G53.2. We probe 12 square degrees of archival data from the UWISH2 survey and identify a total of 127 outflows in these two regions. Using photometric data from multiple Galactic surveys and existing YSO catalogs from the literature, the driving source candidates are identified for 79 outflows (62 % of the total number of outflows identified in the two clouds). The CO velocity-integrated maps for the two clouds show that most of the MHOs identified lie within the cloud boundary, hence, mostly associated with it.

Various estimates of several physical parameters of the MHOs and their driving source candidates have been presented. Physical parameters of 45 driving source candidates have been derived using SED modelling.

The important results obtained from our analysis are summarised below:

- The outflows associated with the two clouds are seen to be predominantly driven by intermediate-mass protostars.
- Outflows have a typical ejection frequency of 1.2 kyr for a typical transversal velocity of 80 kms⁻¹.
- We study and identify various correlations between the physical parameters of the outflow with the physical parameters of the candidate driving source. Despite the scatter observed in our plots, clear trends are seen from the analysis suggesting that brighter YSOs drive more luminous outflows.
- The H₂ 1-0S(1) line flux of outflows is found to be correlated with the length of the outflows. Our results are in agreement with the outflow population of other Galactic plane studies using UWISH2.
- Several interesting star forming regions have been identified based on the spatial distribution of outflows.

Many outflows displaying extended green emission in the IRAC bands, and hence likely EGOs, are identified within the two clouds. These are ideal test laboratories to study massive star formation. We also identify two jets which are spatially located inside the pillars seen in the Vul OB1 complex. One of these outflows inside the pillars is of particular interest and is also characterised by excess extended emission at 4.5 μm along the axis of the outflow. The outflow is driven by a PBR which is an early Class 0 source and is an ideal target to study possible triggered star formation inside a pillar.

Although we discuss various trends and correlations between physical parameters of outflows and their driving source candidates, the scope of our analysis is restricted by the limited data available for the regions. We also acknowledge that, given the lower statistics of outflows driven by Class II and Class III YSOs, the observed trends may be mainly representative of Class 0/I YSOs. Our analysis represents an ideal sample for multi-wavelength analysis employing data from existing as well as upcoming astronomical facilities. Detailed analysis of the special cases discussed will provide a deeper insight into the star formation process and provide clues to address crucial aspects of star formation.

DATA AVAILABILITY

The reduced continuum subtracted H₂ images used in this work are publicly available at the UWISH2 survey archive: <http://astro.kent.ac.uk/uwish2/index.html>. The UKIDSS near-infrared images are publicly available at WSA - WFCAM Science Archive: <http://wsa.roe.ac.uk/>. The Herschel and Spitzer images are publicly available at NASA/IPAC Infrared Science Archive: <https://irsa.ipac.caltech.edu/frontpage/>. All the point source catalog data are publicly available on Vizier. Multiwavelength cutouts of the individual MHOs can be obtained upon reasonable request to the authors.

REFERENCES

- Anglada G., Rodríguez L. F., Carrasco-González C., 2018, *Astronomy and Astrophysics Reviews*, 26, 3
- Arce H. G., Shepherd D., Gueth F., Lee C. F., Bachiller R., Rosen A., Beuther H., 2007, in Reipurth B., Jewitt D., Keil K., eds, *Protostars and Planets V*, p. 245 ([arXiv:astro-ph/0603071](https://arxiv.org/abs/astro-ph/0603071))
- Arce H. G., Borkin M. A., Goodman A. A., Pineda J. E., Halle M. W., 2010, *Astrophysical Journal*, 715, 1170
- Aspin C., Reipurth B., Herczeg G. J., Capak P., 2010, *Astrophysical Journal Letters*, 719, L50
- Audard M., et al., 2014, in Beuther H., Klessen R. S., Dullemond C. P., Henning T., eds, *Protostars and Planets VI*, p. 387 ([arXiv:1401.3368](https://arxiv.org/abs/1401.3368)), doi:10.2458/azu_uapress_9780816531240-ch017
- Bachiller R., 1996, *Annual Review of Astron and Astrophys*, 34, 111
- Bally J., 2016, *Annual Review of Astron and Astrophys*, 54, 491
- Bally J., Reipurth B., Davis C. J., 2007, in Reipurth B., Jewitt D., Keil K., eds, *Protostars and Planets V*, p. 215
- Bate M. R., Bonnell I. A., Clarke C. J., Lubow S. H., Ogilvie G. I., Pringle J. E., Tout C. A., 2000, *Monthly Notices of the Royal Astronomical Society*, 317, 773
- Baug T., et al., 2021, *Monthly Notices of the Royal Astronomical Society*, 507, 4316
- Benjamin R., et al., 2003, *Publications of the Astronomical Society of the Pacific*, 115, 953–964
- Bica E., Bonatto C., Dutra C. M., 2008, *Astronomy and Astrophysics*, 489, 1129
- Billot N., Noriega-Crespo A., Carey S., Guieu S., Shenoy S., Paladini R., Latter W., 2010, *Astrophysical Journal*, 712, 797
- Bonnarel F., et al., 2000, *Astronomy and Astrophysics Supplement*, 143, 33
- Bressan A., Marigo P., Girardi L., Salasnich B., Dal Cero C., Rubele S., Nanni A., 2012, *Monthly Notices of the Royal Astronomical Society*, 427, 127
- Burnham S. W., 1890, *Monthly Notices of the Royal Astronomical Society*, 51, 94
- Caratti o Garatti A., Giannini T., Nisini B., Lorenzetti D., 2006, *Astronomy and Astrophysics*, 449, 1077
- Caratti o Garatti A., Stecklum B., Linz H., García Lopez R., Sanna A., 2015, *Astronomy and Astrophysics*, 573, A82
- Cardelli J. A., Clayton G. C., Mathis J. S., 1989, *Astrophysical Journal*, 345, 245
- Carey S. J., et al., 2009, *Publications of the ASP*, 121, 76
- Chambers E. T., Jackson J. M., Rathborne J. M., Simon R., 2009, *The Astrophysical Journal Supplement Series*, 181, 360
- Churchwell E., et al., 2009, *Publications of the ASP*, 121, 213
- Contreras Peña C., et al., 2017, *Monthly Notices of the Royal Astronomical Society*, 465, 3039
- Contreras Peña C., Naylor T., Morrell S., 2019, *Monthly Notices of the Royal Astronomical Society*, 486, 4590
- Csengeri T., et al., 2014, *Astronomy and Astrophysics*, 565, A75
- Csengeri T., et al., 2016, *Astronomy and Astrophysics*, 586, A149
- Cunningham N. J., Moeckel N., Bally J., 2009, *Astrophysical Journal*, 692, 943
- Cutri R. M., et al. 2012, *VizieR Online Data Catalog*, p. II/311
- Cyganowski C. J., et al., 2008, *Astronomical Journal*, 136, 2391
- Dame T. M., Hartmann D., Thaddeus P., 2001, *Astrophysical Journal*, 547, 792
- Davis C. J., et al., 2009, *Astronomy and Astrophysics*, 496, 153
- Davis C. J., Gell R., Khanzadyan T., Smith M. D., Jenness T., 2010, *Astronomy and Astrophysics*, 511, A24
- Dunham M. M., et al., 2006, *Astrophysical Journal*, 651, 945
- Dunham M. M., Crapsi A., II N. J. E., Bourke T. L., Huard T. L., Myers P. C., Kauffmann J., 2008, *The Astrophysical Journal Supplement Series*, 179, 249
- Dunham M. M., Arce H. G., Bourke T. L., Chen X., van Kempen T. A., Green J. D., 2012, *Astrophysical Journal*, 755, 157
- Falle S. A. E. G., Raga A. C., 1993, *Monthly Notices of the Royal Astronomical Society*, 261, 573
- Federrath C., Schrön M., Banerjee R., Klessen R. S., 2014, *Astrophysical Journal*, 790, 128
- Fernández-López M., Girart J. M., Curiel S., Zapata L. A., Fonfría J. P., Qiu K., 2013, *Astrophysical Journal*, 778, 72
- Fischer W. J., Safron E., Megeath S. T., 2019, *Astrophysical Journal*, 872, 183
- Froebrich D., Makin S. V., 2016, *Monthly Notices of the Royal Astronomical Society*, 462, 1444
- Froebrich D., et al., 2011, *Monthly Notices of the Royal Astronomical Society*, 413, 480–492
- Froebrich D., et al., 2015, *Monthly Notices of the Royal Astronomical Society*, 454, 2586

- Greene T. P., Wilking B. A., Andre P., Young E. T., Lada C. J., 1994, *Astrophysical Journal*, 434, 614
- Gutermuth R. A., Heyer M., 2015, *Astronomical Journal*, 149, 64
- Hales A. S., et al., 2020, *Astrophysical Journal*, 900, 7
- Hanson M. M., Luhman K. L., Rieke G. H., 2002, *The Astrophysical Journal Supplement Series*, 138, 35
- Haro G., 1952, *Astrophysical Journal*, 115, 572
- Hartigan P., Reiter M., Smith N., Bally J., 2015, *Astronomical Journal*, 149, 101
- Hartmann L., Kenyon S. J., 1985, *Astrophysical Journal*, 299, 462
- Hartmann L., Calvet N., Gullbring E., D'Alessio P., 1998, *Astrophysical Journal*, 495, 385
- Herbig G. H., 1950, *Astrophysical Journal*, 111, 11
- Herczeg G. J., et al., 2017, *Astrophysical Journal*, 849, 43
- Ioannidis G., Froebrich D., 2012a, *Monthly Notices of the Royal Astronomical Society*, 421, 3257–3265
- Ioannidis G., Froebrich D., 2012b, *Monthly Notices of the Royal Astronomical Society*, 425, 1380
- Jackson J. M., et al., 2006, *The Astrophysical Journal Supplement Series*, 163, 145
- Kenyon S. J., Hartmann L. W., Strom K. M., Strom S. E., 1990, *Astronomical Journal*, 99, 869
- Kim H.-J., Koo B.-C., Davis C. J., 2015, *Astrophysical Journal*, 802, 59
- Kohno M., et al., 2022, *Publications of the ASJ*, 74, 24
- Kong S., Arce H. G., Maureira M. J., Caselli P., Tan J. C., Fontani F., 2019, *Astrophysical Journal*, 874, 104
- Krumholz M. R., Federrath C., 2019, *Frontiers in Astronomy and Space Sciences*, 6, 7
- Lada C. J., 1987, in Peimbert M., Jugaku J., eds, Vol. 115, *Star Forming Regions*. p. 1
- Lee C.-F., 2020, *Astronomy and Astrophysics Reviews*, 28, 1
- Li Q., et al., 2018, *Astrophysical Journal*, 867, 167
- Lucas P. W., et al., 2008, *Monthly Notices of the Royal Astronomical Society*, 391, 136
- Machida M. N., Basu S., 2019, *Astrophysical Journal*, 876, 149
- Machida M. N., Hosokawa T., 2013, *Monthly Notices of the Royal Astronomical Society*, 431, 1719
- Makin S. V., 2019, PhD thesis, University of Kent
- Makin S. V., Froebrich D., 2018, *The Astrophysical Journal Supplement Series*, 234, 8
- Manoj P., et al., 2013, *Astrophysical Journal*, 763, 83
- Maury A. J., André P., Li Z. Y., 2009, *Astronomy and Astrophysics*, 499, 175
- Meingast S., Lombardi M., Alves J., 2017, *Astronomy and Astrophysics*, 601, A137
- Molinari S., et al., 2010, *Publications of the Astronomical Society of the Pacific*, 122, 314–325
- Molinari S., et al., 2016, *Astronomy and Astrophysics*, 591, A149
- Morales E. F. E., Wyrowski F., Schuller F., Menten K. M., 2013, *Astronomy and Astrophysics*, 560, A76
- Murray D., Goyal S., Chang P., 2018, *Monthly Notices of the Royal Astronomical Society*, 475, 1023
- Nakamura F., Li Z.-Y., 2007, *Astrophysical Journal*, 662, 395
- Nakamura F., et al., 2011, *Astrophysical Journal*, 737, 56
- Nony T., et al., 2020, *Astronomy and Astrophysics*, 636, A38
- Offner S. S. R., Arce H. G., 2014, *Astrophysical Journal*, 784, 61
- Offner S. S. R., McKee C. F., 2011, *Astrophysical Journal*, 736, 53
- Panwar N., Samal M. R., Pandey A. K., Singh H. P., Sharma S., 2019, *Astronomical Journal*, 157, 112
- Park W., et al., 2021, *Astrophysical Journal*, 920, 132
- Plunkett A. L., Arce H. G., Corder S. A., Mardones D., Sargent A. I., Schnee S. L., 2013, *Astrophysical Journal*, 774, 22
- Ray T. P., Ferreira J., 2021, *New Astronomy Review*, 93, 101615
- Reed B. C., 2003, *Astronomical Journal*, 125, 2531
- Reipurth B., Bally J., 2001, *Annual Review of Astron and Astrophys*, 39, 403
- Reipurth B., Bally J., Devine D., 1997, *Astronomical Journal*, 114, 2708
- Reipurth B., Yu K. C., Rodríguez L. F., Heathcote S., Bally J., 1999, *Astronomy and Astrophysics*, 352, L83
- Reipurth B., Yu K. C., Moriarty-Schieven G., Bally J., Aspin C., Heathcote S., 2004, *Astronomical Journal*, 127, 1069
- Reiter M., Kiminki M. M., Smith N., Bally J., 2017, *Monthly Notices of the Royal Astronomical Society*, 470, 4671
- Reiter M., Morse J. A., Smith N., Haworth T. J., Kuhn M. A., Klaassen P. D., 2022, *Monthly Notices of the Royal Astronomical Society*, 517, 5382
- Robitaille T. P., 2017, *Astronomy and Astrophysics*, 600, A11
- Robitaille T. P., Whitney B. A., Indebetouw R., Wood K., Denzmore P., 2006, *The Astrophysical Journal Supplement Series*, 167, 256
- Rohde P. F., Walch S., Seifried D., Whitworth A. P., Clarke S. D., Hubber D. A., 2019, *Monthly Notices of the Royal Astronomical Society*, 483, 2563
- Rosen A. L., Krumholz M. R., 2020, *Astronomical Journal*, 160, 78
- Samal M. R., Chen W. P., Takami M., Jose J., Froebrich D., 2018, *Monthly Notices of the Royal Astronomical Society*, 477, 4577–4595
- Scholz A., Froebrich D., Wood K., 2013, *Monthly Notices of the Royal Astronomical Society*, 430, 2910
- Schuller F., et al., 2009, *Astronomy and Astrophysics*, 504, 415
- Sharpless S., 1959, *The Astrophysical Journal Supplement Series*, 4, 257
- Snell R. L., Loren R. B., Plambeck R. L., 1980, *Astrophysical Journal, Letters*, 239, L17
- Spitzer Science C., 2009, *VizieR Online Data Catalog*, p. II/293
- Stahler S. W., Palla F., 2004, *The Formation of Stars*
- Stanke T., McCaughrean M. J., Zinnecker H., 2002, *Astronomy and Astrophysics*, 392, 239
- Stutz A. M., et al., 2013, *Astrophysical Journal*, 767, 36
- Szegedi-Elek E., et al., 2020, *Astrophysical Journal*, 899, 130
- Takami M., et al., 2020, *Astrophysical Journal*, 901, 24
- Terquem C., Eisloffel J., Papaloizou J. C. B., Nelson R. P., 1999, *Astrophysical Journal, Letters*, 512, L131
- Varricatt W. P., Davis C. J., Ramsay S., Todd S. P., 2010, *Monthly Notices of the Royal Astronomical Society*, 404, 661
- Varricatt W. P., Thomas H. S., Davis C. J., Ramsay S., Currie M. J., 2013, *Astronomy and Astrophysics*, 554, A9
- Verliat A., Hennebelle P., González M., Lee Y.-N., Geen S., 2022, *Astronomy and Astrophysics*, 663, A6
- Vorobyov E. I., Basu S., 2015, *Astrophysical Journal*, 805, 115
- Vorobyov E. I., Elbakyan V. G., Plunkett A. L., Dunham M. M., Audard M., Guedel M., Dionatos O., 2018, *Astronomy and Astrophysics*, 613, A18
- Wang P., Li Z.-Y., Abel T., Nakamura F., 2010, *Astrophysical Journal*, 709, 27
- Wang Y., et al., 2020, *Astronomy and Astrophysics*, 641, A53
- Wolf-Chase G., Arvidsson K., Smutko M., 2017, *Astrophysical Journal*, 844, 38
- Zakri W., et al., 2022, *Astrophysical Journal, Letters*, 924, L23
- Zhang M., et al., 2013, *Astronomy and Astrophysics*, 553, A41
- Zhang M., Fang M., Wang H., Sun J., Wang M., Jiang Z., Anathipindika S., 2015, *The Astrophysical Journal Supplement Series*, 219, 21
- Zinchenko I., et al., 2015, *Astrophysical Journal*, 810, 10

SUPPORTING INFORMATION

Additional Supporting Information may be found in the online version of this article:

APPENDIX A: Full list of MHO and YSO parameters as provided in Table 1 and Table 2

APPENDIX B: Images of MHOs identified in the study region.